

Terahertz-field-induced carrier generation in $\text{Bi}_{1-x}\text{Sb}_x$ Dirac electron systemsI. Katayama,¹ H. Kawakami,¹ T. Hagiwara,¹ Y. Arashida,¹ Y. Minami,^{1,2} L.-W. Nien,³ O. S. Handegard,^{3,4} T. Nagao,^{3,4} M. Kitajima,^{1,3} and J. Takeda¹¹*Yokohama National University, Tokiwadai 79-5, Hodogaya-ku, Yokohama 240-8501, Japan*²*Tokushima University, Minami-Josanjima 2-1, Tokushima 770-8506, Japan*³*National Institute for Materials Science (NIMS), Namiki 1-1, Tsukuba 305-0044, Japan*⁴*Hokkaido University, Kita 10, Nishi 8, Kita-ku, Sapporo 060-0810, Japan*

(Received 12 May 2018; revised manuscript received 29 October 2018; published 3 December 2018)

Terahertz-field-induced carrier generation processes were investigated in Dirac electron systems, single-crystalline bismuth antimony alloy thin films ($\text{Bi}_{1-x}\text{Sb}_x$; $0 \leq x \leq 0.16$). This investigation was performed by precisely tuning, via the substituent ratio x , the band structure of the films from that associated with a semimetal to that characteristic of a narrow-gap semiconductor. Terahertz-field-induced absorption was clearly observed within a few picoseconds after the terahertz pump-pulse illumination of $\text{Bi}_{1-x}\text{Sb}_x$ semimetal and semiconductor samples. The field-strength dependence of the induced absorption was compared with the calculated Zener tunneling probability in the Dirac-like band dispersion. Through this comparison, the mechanism of the induced absorption was attributed to the carrier generation via the terahertz-field-induced Zener tunneling. The tunneling occurred in subpicosecond timescales even at room temperature, demonstrating that $\text{Bi}_{1-x}\text{Sb}_x$ thin films are promising for future high-speed electronics and the investigation of universal ultrafast tunneling dynamics.

DOI: [10.1103/PhysRevB.98.214302](https://doi.org/10.1103/PhysRevB.98.214302)**I. INTRODUCTION**

The strong interaction between light and matter yields many exotic nonlinear phenomena (such as high-harmonics generation, carrier multiplication due to impact ionization, and field-induced Zener tunneling between valence and conduction bands) in solid states [1–4]. These nonlinear phenomena hold enormous promise for future high-speed nonlinear optoelectronic devices operated at terahertz and petahertz ranges of frequency [5,6]. The use of nonlinear carrier generation processes such as Zener tunneling is one of the keys to realize the ultrafast devices, and therefore, fundamental understanding of the process is highly desired [7–11]. Furthermore, the field-induced Zener tunneling in Dirac electron systems would arouse great interest in relation to quantum electrodynamics (QED) in strong electric fields; electron-hole pair generation induced via Zener tunneling is analogous to the generation of a strong-field-induced electron-positron pair in vacuum [12]. To date, however, the carrier generation process occurring via Zener tunneling was not fully examined in comparison with that via the impact ionization [13,14], and therefore, a systematic investigation of Zener tunneling in a typical Dirac electron system is essential to understand the underlying physics such as the field-induced tunneling dynamics, which may depend on the electronic structure from a semimetal to a narrow-gap semiconductor.

The nonlinear interaction between light and matter is generally characterized by the Keldysh parameter $\gamma = \sqrt{E_g/2U_p}$, where E_g and U_p are the band-gap energy and the ponderomotive energy, respectively. If $\gamma > 1$, the perturbative multiphoton ionization process dominates the observed optical nonlinearity and if $\gamma < 1$, the nonperturbative field-induced tunneling process becomes significant [15]. Since

the Keldysh parameter is proportional to $\sqrt{E_g}$, the critical electric-field strength across the crossover from the perturbative to nonperturbative regime decreases in the case of narrow-gap semiconductors and semimetals [11]. These materials are therefore promising candidates for investigating the nonperturbative nonlinear carrier generation processes occurring in materials. Here, we demonstrate that illumination of bismuth antimony alloys ($\text{Bi}_{1-x}\text{Sb}_x$; $0 \leq x \leq 0.16$) by intense terahertz electric fields provides a suitable platform for unveiling extremely nonlinear carrier generation processes in Dirac electron systems. The applied terahertz electric fields can either accelerate or generate carriers effectively at the picosecond timescale before interband relaxation and heat transfer to the lattice occurs.

Figure 1(a) schematically illustrates the band structure of $\text{Bi}_{1-x}\text{Sb}_x$ as a function of the substituent ratio x , where the dashed line shows the chemical potential μ . In pure Bi, the band structure around the L point of the first Brillouin zone is well approximated by the Wolff Hamiltonian (anisotropic Dirac Hamiltonian), with band-gap energy on the order of a few tens of meV [16]. This structure also has a hole pocket at the T point with a relatively large effective mass and band gap [17]. Consequently, electrons in the L point with a low effective mass contribute mainly to the field-induced carrier dynamics [16,18]. The use of $\text{Bi}_{1-x}\text{Sb}_x$ thin films allows us to precisely tune, via the substituent ratio x , the band-gap energy from values characteristic of a semimetal ($0 \leq x \leq 0.09$) to values associated with a narrow-gap semiconductor ($0.09 \leq x \leq 0.16$). The Dirac-like asymptotic linear band structure is maintained despite the change in the band-gap energy. Hence, $\text{Bi}_{1-x}\text{Sb}_x$ thin films are well suited for our study of elucidating a nonlinear carrier generation mechanism in Dirac electron systems.

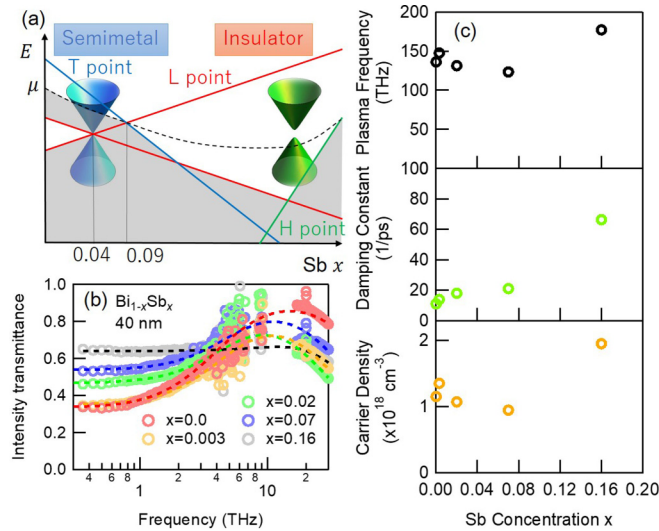


FIG. 1. (a) Schematic showing dependence of the chemical potential μ and the energy of high-symmetry points in the Brillouin zone on the Sb concentration. Insulating thin films will be formed at Sb concentrations exceeding $x = 0.09$. (b) Terahertz and infrared transmission spectra of 40-nm-thick $\text{Bi}_{1-x}\text{Sb}_x$ thin films (for several Sb concentrations) with respect to that of the bare Si substrate. Data below 10 THz are measured with a terahertz time-domain spectroscopy (TDS) setup, and the rest are obtained with a conventional Fourier transform infrared (FTIR) spectrometer. Dashed lines indicate the results of Drude fitting [the corresponding parameters are shown in (c)]. (c) Dependence of the plasma frequency, damping constant, and carrier density on the Sb concentration.

II. EXPERIMENT

Using molecular beam epitaxy, we prepared high-quality $\text{Bi}_{1-x}\text{Sb}_x$ ($0 \leq x \leq 0.16$) epitaxial thin films (thickness: 40 nm) deposited on a (7×7) reconstructed surface of a high-resistivity silicon (Si) (111) substrate [19–21]. Details of the sample preparation and the experimental setups are described in the Supplemental Material [22]. Figure 1(b) shows the terahertz transmittance measured at weak electric-field strengths within the linear regime of different Sb composition rates [23]. The transmittance below 10 THz increases with increasing Sb concentration, suggesting that the absorption due to free electrons decreases with increasing Sb concentration. Moreover, the plasma frequency, damping constant, and carrier density were obtained [see dashed lines in Fig. 1(c)] based on the Drude analysis described in the Supplemental Material [22]. The carrier density decreases as the band structure approaches the region where the $\text{Bi}_{1-x}\text{Sb}_x$ becomes semiconducting. The increase in the carrier concentration at $x = 0.16$ may be attributed to the contribution from the H point holes, as shown in Fig. 1(a).

III. EXPERIMENTAL RESULTS

To examine terahertz-field-induced carrier generation processes in $\text{Bi}_{1-x}\text{Sb}_x$ thin films, we measured the dependence of the terahertz transmittance on the peak electric-field strength [24,25]. Figure 2 shows the typical results obtained for the terahertz-field-induced transmittance of $\text{Bi}_{1-x}\text{Sb}_x$

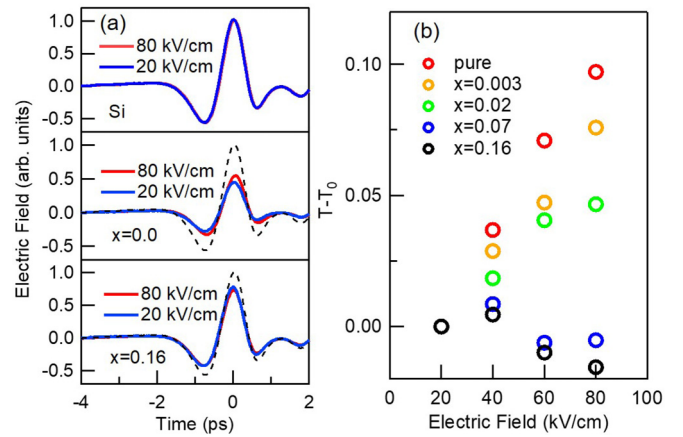


FIG. 2. (a) Comparison of the terahertz waveforms transmitted through the reference Si substrate, pure Bi ($x = 0$), and $\text{Bi}_{1-x}\text{Sb}_x$ ($x = 0.16$) samples at two different field strengths. Dashed lines in the middle and lower graphs indicate the reference waveforms. (b) Dependence of the terahertz transmittance averaged over 0.35–1.0 THz on the peak terahertz field strength. Data for several Sb concentrations are shown for comparison of the nonlinearity.

thin films with different Sb concentrations. The transmittance of the semimetal samples (typically, $x = 0$) increases with increasing electric-field strength [see Fig. 2(a)], owing to the terahertz-field-induced acceleration of the Dirac electrons [26]. In contrast, the transmittance of the semiconducting samples (typically, $x = 0.16$) decreases slightly with increasing field strength. A plot of the terahertz-field-induced transmittance as a function of the electric-field strength [see Fig. 2(b)] reveals the differing field dependence of the semimetal ($0 \leq x \leq 0.02$) and semiconductor ($0.07 \leq x \leq 0.16$) samples. As discussed below, the transmittance of the semiconducting samples is attributed to a nonlinear mechanism other than the carrier acceleration [26].

To reveal the mechanism governing this field-induced absorption, we perform terahertz-pump and terahertz-probe spectroscopy using the experimental optical setup described in the Supplemental Material [22]. The electric-field strength of the probe employed in this experiment is relatively low and, hence, nonlinearity in the samples is avoided. Figures 3(a) and 3(b) show the typical results obtained for the terahertz transmittance as a function of the time interval between the pump and probe terahertz pulses. In the semimetal samples ($x = 0$ and 0.02), we found that the terahertz-induced transparency occurs at the time origin, owing to the terahertz-field-induced acceleration of conduction electrons. In other words, the conduction electrons are accelerated via intense terahertz electric fields along the Dirac-like asymptotic linear band dispersion with an increase in the electron effective masses [26]. Subsequently, the terahertz-induced absorption emerges with a decay time of about 10 ps after the terahertz illumination, implying that field-induced carrier generation and relaxation occur in the samples. This absorption occurred in both the semimetal and semiconductor samples, suggesting that the origin of the observed absorption is universal in Dirac electron systems.

To elucidate the relaxation dynamics of the induced absorption, we analyze the data between 2 and 8 ps using

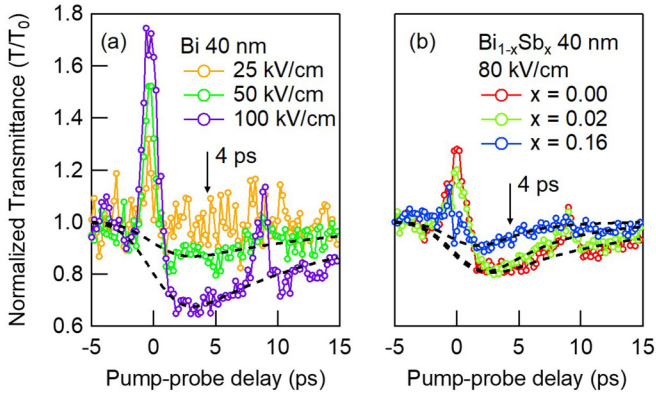


FIG. 3. Delay dependence of the terahertz-pump and terahertz-probe signals for (a) pure Bi with different electric-field strengths and for (b) different Sb concentrations. We plotted the ratio of average terahertz transmittance from 0.35 to 1.0 THz normalized by that obtained without the terahertz-pump pulse. The second peaks that appear at 8 ps correspond to the reflection from the back surface of the Si substrate. The arrow at 4 ps indicates the delay time where the field dependence at different Sb concentrations is measured, as shown in Fig. 4. Dashed lines are the best fits obtained by the method as described in the main text. Note that the scale values of the vertical axis in (a,b) are the same.

an exponential decay function convoluted with a Gaussian function as follows. The Gaussian function was chosen for simplicity.

$$\Delta T(t) \propto \int_{-\infty}^t dt' \exp\left(-\frac{t-t'}{\tau} - \frac{t'^2}{2\sigma^2}\right).$$

Here, τ is the relaxation time, and $\sigma = 2$ ps is the pulse duration of the terahertz wave. The dashed lines in Figs. 3(a) and 3(b) represent the best fits with $\tau = 10$ ps ($x = 0$), 4.9 ps ($x = 0.02$), and 2.9 ps ($x = 0.16$). The observed relaxation times are comparable to that observed in the previously reported optical-pump and terahertz-probe experiment (4 ps) [27]. The faster relaxation time with the Sb concentration may originate from the increase of either intervalley scattering due to phonons or inhomogeneity. The amplitude of induced transmittance change also depends on the Sb concentration. To explain the terahertz-field-induced dynamics observed both in semimetallic and semiconducting samples, we will discuss two possible mechanisms in the Dirac electron systems as shown in Fig. 4(a) in the following: i.e., Zener tunneling and impact ionization.

IV. CALCULATION AND DISCUSSION

For Zener tunneling, the tunneling probability of the Dirac system is determined from [28]:

$$P_{\text{Zener}}(F) = \exp\left[-\frac{\pi}{4} \frac{E_g^2(k)}{\hbar c e F}\right].$$

Here, $E(k) = \sqrt{E_g^2 + \hbar^2 c^2 k^2}$ is the band-gap energy with a wave vector k ; c and F are the asymptotic velocity of the Dirac system (the so-called effective light velocity of the system) and the applied electric field, respectively. In the cal-

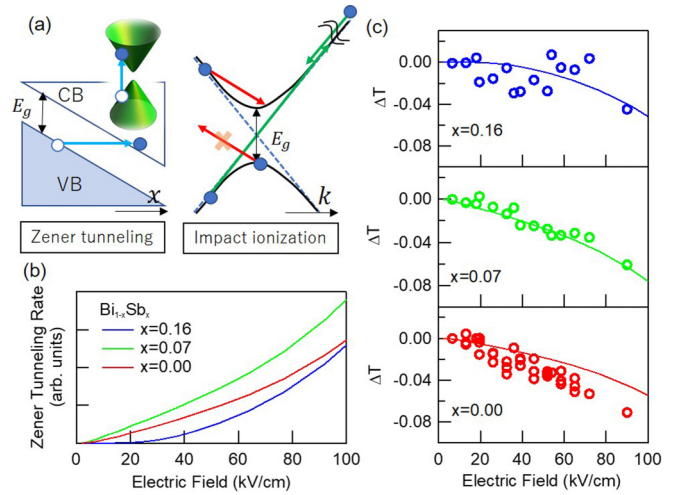


FIG. 4. (a) Schematic of Zener tunneling and impact ionization processes occurring in the Dirac band structure. Solid and open circles in the left indicate the electrons and holes excited by the Zener tunneling (the blue arrows) depicted in both the real and momentum spaces. Solid circles in the right indicate the initial states of the impact ionization. In the case of the scattering wave vector shown as the red arrow, the valence electron could not be excited because of the absence of the final state satisfying energy-momentum conservation. In the case shown as the green arrows, the energy and momentum conservation rule is approximately satisfied, as the energy-momentum dispersion can be approximated by the Dirac cone at high energy. CB: conduction band, VB: valence band. (b) Calculated field dependence of the Zener tunneling rate for different Sb concentrations. (c) Dependence of the transmittance change in the terahertz-pump and terahertz-probe measurement (time delay: 4 ps) on the electric field strength. The solid lines are the calculation results shown in (b) normalized by the data for $x = 0.07$.

ulation, we used the well-known empirical values of the band-gap energy and Fermi energy for each $\text{Bi}_{1-x}\text{Sb}_x$ sample, taken from Ref. [16,22]. To obtain the probability per unit time, we define an attempt frequency $\alpha(F) = aeF/\hbar$, which describes the frequency of band electrons to attempt the tunneling at each wave vector (a : lattice constant of Bi) [29]. The wave vector of the electrons should be conserved between the initial and final states and, hence, the Zener tunneling is regarded as the vertical transition between the valence and the conduction bands, as illustrated by the blue arrow in Fig. 4(a) [9]. Subsequently, the tunneling probability from the valence to the conduction band can be obtained by integrating over the entire Brillouin zone [7].

When calculating the tunneling probability, for simplicity, we consider an isotropic Dirac band [16], and assume that the intraband electron-electron scattering is sufficiently rapid to ensure the thermal equilibrium of each Dirac band. The number of electrons generated via the Zener tunneling can then be expressed as

$$N(F) = \int dk f_v(k)[1 - f_c(k)]\alpha(F)P_{\text{Zener}}(F),$$

where $f_{v,c}(k)$ represents the Fermi-Dirac distribution function at wave vector k for valence and conduction band, respectively. The calculated field-strength dependence of the tun-

neling electron rate is summarized in Fig. 4(b), where the dependence varies with Sb concentration.

Since the Zener tunneling rate will be proportional to the number of generated carriers, the calculated tunneling rates can be directly compared with the experimental results shown in Fig. 3. The absorption strength is experimentally estimated at the pump-probe delay time of 4 ps, where the conduction electron acceleration or the field-induced transparency can be completely neglected. In the comparison, the proportionality constant relating the calculated tunneling rate to the induced absorption is adjusted with the experimental data for $x = 0.07$ [see Fig. 4(c)]. As the figure shows, satisfactory agreement is obtained between the calculated values and the experimental values. This agreement is obtained although the band gap and Fermi level of the $\text{Bi}_{1-x}\text{Sb}_x$ Dirac electron systems change from those characterizing a semimetal to those characterizing a semiconductor, as shown in Fig. 1(a) (the details of the dependence are shown in the Supplemental Material [22] and Ref. [16]). The agreement realized for the entire range of substitution ratio x values and the small Keldysh parameter for $\text{Bi}_{1-x}\text{Sb}_x$ films (e.g., $\gamma = 0.02$ for pure bismuth at 100 kV/cm and 1 THz) strongly indicates that Zener tunneling plays a key role in the observed terahertz-induced absorption.

For the impact ionization process, a hot conduction electron interacts with a valence electron through the Coulomb interaction under energy and momentum conservation. However, energy or momentum conservation may be violated in Dirac electron systems with a finite effective mass, as indicated by red arrows in Fig. 4(a). Energy and momentum conservation requires, as indicated by green arrows, an anomalous acceleration of the carriers in the Dirac-like band toward much higher energy than the band-gap energy [14,27]. This acceleration is, however, unrealistic under the present experimental conditions [26]. Although the impact ionization process assisted by either phonons or inhomogeneity might be another possibility under the violation of energy and momentum conservation, the estimated small Keldysh parameter for our experimental condition indicates the dominant contribution of the Zener tunneling. Furthermore, the long Fermi wavelength [30] of $\text{Bi}_{1-x}\text{Sb}_x$ would make the impact ionization mediated by the inhomogeneity less favorable, because the electrons with the long wavelength become insensitive to the inhomogeneity on the atomic scale.

Figure 5 illustrates the dynamics in $\text{Bi}_{1-x}\text{Sb}_x$ induced by intense terahertz transients. The intense terahertz electric field induces both the acceleration of the Dirac electrons and the carrier generation due to the Zener tunneling. The excited carriers reach the thermal equilibrium within 1–2 ps, and then relax to the initial state within 10 ps. Although Zener tunneling is a well-established mechanism, the results are important in the field of strong light-matter physics, owing to the following reasons. First, the use of intense terahertz electric-field transients can distinguish the field-induced carrier generation from other undesirable effects (e.g., interband scattering) and thermal effects in the time domain, as demonstrated in this study. Second, $\text{Bi}_{1-x}\text{Sb}_x$ becomes a prototypical Dirac electron system, which can easily tune the band-gap energy from that of a semimetal to that of a narrow-gap

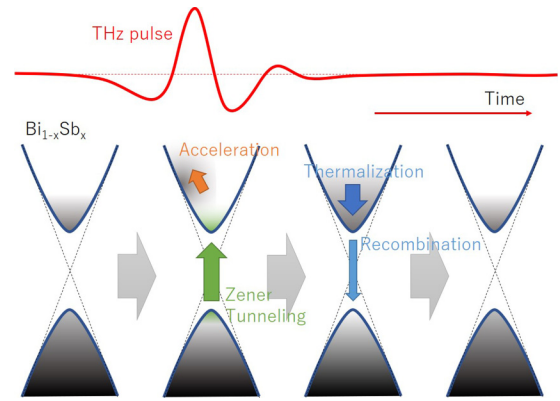


FIG. 5. Schematic of carrier generation and relaxation processes in $\text{Bi}_{1-x}\text{Sb}_x$ Dirac electron systems. The acceleration of electrons in the conduction band as well as the Zener tunneling is simultaneously induced via the terahertz pulses at around the intense peak electric field. Subsequently, the generated carriers in the conduction and valence bands gradually relax to the initial states via the thermalization and recombination processes within 10 ps.

semiconductor by changing the substituent ratio x . The Dirac-like asymptotic linear band structure is maintained despite this change. Moreover, a reduction in the influence of defects or impurities (which have a significant effect on the dynamics in the case of wide-gap semiconductors) is expected in the case of narrow-gap semiconductors. These technical merits hold enormous promise for future elaborate investigation of Dirac electrons under the strong light-matter interaction, which may unveil inherent nonlinear characteristics of Dirac electron systems [31].

V. CONCLUSION

In conclusion, we measured the nonlinear terahertz responses of Bi and $\text{Bi}_{1-x}\text{Sb}_x$ single-crystalline thin films, by investigating the nonlinear terahertz transmittance and terahertz-induced absorption via terahertz-pump and -probe spectroscopy. When we increase the intensity of the pump terahertz wave, the intensity dependence of the terahertz absorption obtained for the semimetal samples differs from that obtained for the semiconductor samples. Terahertz-pump and terahertz-probe spectroscopy revealed that this absorption originates from the Zener tunneling in the Dirac systems, which is also supported by calculated results. Since the band structure and Fermi energy can be tuned via Sb doping, the $\text{Bi}_{1-x}\text{Sb}_x$ systems could be an interesting platform for investigating the strong light-matter interactions in Dirac systems.

ACKNOWLEDGMENTS

The authors acknowledge the financial support for this work by JSPS, Grant-in-Aid for Scientific Research (KAKENHI Grants No. 18H04288, No. 17H06124, No. 16H03820, No. 16H04001, and No. 16H06364) and by JST, CREST (Grant No. JPMJCR13C3).

- [1] O. Schubert, M. Hohenleutner, F. Langer, B. Urbanek, C. Lange, U. Huttner, D. Golde, T. Meier, M. Kira, S. W. Koch, and R. Huber, *Nat. Photonics* **8**, 119 (2014).
- [2] H. Hirori, K. Shinokita, M. Shirai, S. Tani, Y. Kadoya, and K. Tanaka, *Nat. Commun.* **2**, 594 (2011).
- [3] A. Schiffrin, T. Paasch-Colberg, N. Karpowicz, V. Apalkov, D. Gerster, S. Muhlbrandt, M. Korbman, J. Reichert, M. Schultze, S. Holzner, J. V. Barth, R. Kienberger, R. Ernstorfer, V. S. Yakovlev, M. I. Stockman, and F. Krausz, *Nature* **493**, 70 (2013).
- [4] N. Yoshikawa, T. Tamaya, and K. Tanaka, *Science* **356**, 736 (2017).
- [5] F. Junginger, B. Mayer, C. Schmidt, O. Schubert, S. Mahrlein, A. Leitenstorfer, R. Huber, and A. Pashkin, *Phys. Rev. Lett.* **109**, 147403 (2012).
- [6] H. Mashiko, K. Oguri, T. Yamaguchi, A. Suda, and H. Gotoh, *Nat. Phys.* **12**, 741 (2016).
- [7] E. O. Kane, *J. Phys. Chem. Solids* **12**, 181 (1960).
- [8] T. Tamaya, A. Ishikawa, T. Ogawa, and K. Tanaka, *Phys. Rev. Lett.* **116**, 016601 (2016).
- [9] G. Kane, M. Lazzeri, and F. Mauri, *J. Phys. Condens. Matter* **27**, 164205 (2015).
- [10] H. Yamakawa, T. Miyamoto, T. Morimoto, T. Terashige, H. Yada, N. Kida, M. Suda, H. M. Yamamoto, R. Kato, K. Miyagawa, K. Kanoda, and H. Okamoto, *Nat. Mater.* **16**, 1100 (2017).
- [11] T. Higuchi, C. Heide, K. Ullmann, H. B. Weber, and P. Hommelhoff, *Nature* **550**, 224 (2017).
- [12] T. Oka and H. Aoki, *Phys. Rev. Lett.* **95**, 137601 (2005).
- [13] M. C. Hoffmann, J. Hebling, H. Y. Hwang, K.-L. Yeh, and K. A. Nelson, *Phys. Rev. B* **79**, 161201(R) (2009).
- [14] S. Tani, F. Blanchard, and K. Tanaka, *Phys. Rev. Lett.* **109**, 166603 (2012).
- [15] K. Tanaka, H. Hirori, and M. Nagai, *IEEE Trans. Terahertz Sci. Technol.* **1**, 301 (2011).
- [16] Y. Fuseya, M. Ogata, and H. Fukuyama, *J. Phys. Soc. Jpn.* **84**, 012001 (2015).
- [17] Z. Zhu, B. Fauqué, Y. Fuseya, and K. Behnia, *Phys. Rev. B* **84**, 115137 (2011).
- [18] D. Hsieh, D. Qian, L. Wray, Y. Xia, Y. S. Hor, R. J. Cava, and M. Z. Hasan, *Nature* **452**, 970 (2008).
- [19] T. Hirahara, T. Nagao, I. Matsuda, G. Bihlmayer, E. V. Chulkov, Y. M. Koroteev, P. M. Echenique, M. Saito, and S. Hasegawa, *Phys. Rev. Lett.* **97**, 146803 (2006).
- [20] T. Nagao, J. T. Sadowski, M. Saito, S. Yaginuma, Y. Fujikawa, T. Kogure, T. Ohno, Y. Hasegawa, S. Hasegawa, and T. Sakurai, *Phys. Rev. Lett.* **93**, 105501 (2004).
- [21] S. Ito, B. Feng, M. Arita, A. Takayama, R. Y. Liu, T. Someya, W. C. Chen, T. Iimori, H. Namatame, M. Taniguchi, C. M. Cheng, S. J. Tang, F. Komori, K. Kobayashi, T. C. Chiang, and I. Matsuda, *Phys. Rev. Lett.* **117**, 236402 (2016).
- [22] See Supplemental Material at <http://link.aps.org/supplemental/10.1103/PhysRevB.98.214302>, which includes Refs. [19,20] for sample preparation, Ref. [23] for the linear terahertz spectrometer, and Refs. [24,25] for the nonlinear terahertz spectrometer.
- [23] K. Yokota, J. Takeda, C. Dang, G. Han, D. N. McCarthy, T. Nagao, S. Hishita, M. Kitajima, and I. Katayama, *Appl. Phys. Lett.* **100**, 251605 (2012).
- [24] J. Hebling, G. Almási, I. Z. Kozma, and J. Kuhl, *Opt. Express* **10**, 1161 (2002).
- [25] H. Hirori, A. Doi, F. Blanchard, and K. Tanaka, *Appl. Phys. Lett.* **98**, 091106 (2011).
- [26] Y. Minami, K. Araki, T. D. Dao, T. Nagao, M. Kitajima, J. Takeda, and I. Katayama, *Sci. Rep.* **5**, 15870 (2015).
- [27] I. Timrov, T. Kampfrath, J. Faure, N. Vast, C. R. Ast, C. Frischkorn, M. Wolf, P. Gava, and L. Perfetti, *Phys. Rev. B* **85**, 155139 (2012).
- [28] D. Jena, T. Fang, Q. Zhang, and H. Xing, *Appl. Phys. Lett.* **93**, 112106 (2008).
- [29] C. Zener, *Proc. R. Soc. London, Ser. A* **145**, 523 (1934).
- [30] K. Behnia, L. Balicas, and Y. Kopelevich, *Science* **317**, 1729 (2007).
- [31] J. Reimann, S. Schlauderer, C. P. Schmid, F. Langer, S. Baierl, K. A. Kokh, O. E. Tereshchenko, A. Kimura, C. Lange, J. GÜdde, U. Höfer, and R. Huber, *Nature* **562**, 396 (2018).

Supplemental materials for “Terahertz-Field-Induced Zener Tunneling in $\text{Bi}_{1-x}\text{Sb}_x$ Dirac Electron Systems”

I. Katayama¹, H. Kawakami¹, Y. Arashida¹, Y. Minami^{1,2}, O. S. Handegard^{3,4},
L.-W. Nien³, T. Nagao^{3,4}, M. Kitajima^{1,3}, and J. Takeda¹

¹ *Yokohama National University, Yokohama 240-8501, Japan*

² *Tokushima University, Minami-Josanjima 2-1, Tokushima 770-8506, Japan*

³ *National Institute for Materials Science (NIMS), Namiki 1-1, Tsukuba, Ibaraki
305-0044, Japan*

⁴ *Hokkaido University, Kita 10, Nishi 8, Kita-ku, Sapporo 060-0810, Japan*

(Dated:)

1. Sample preparation

We prepared high-quality single-crystalline $\text{Bi}_{1-x}\text{Sb}_x$ ($0 \leq x \leq 0.16$) epitaxially grown thin films with thickness of about 40 nm deposited on (7×7) reconstructed surface of a high resistivity Si (111) substrate using molecular beam epitaxy (MBE) [1-3]. The base pressure of the MBE chamber was below 1.0×10^{-7} Pa. The evaporation rates for Bi and Sb were checked in advance to the deposition to roughly determine the Sb concentration x . The total evaporation rate was set below 0.05 nm/min. to keep the high crystallinity of the sample. After the crystal growth, we annealed the sample at 350 K for 10 minutes. The crystallinity was in-situ monitored by reflection high-energy electron diffraction (RHEED). The Sb composition x and the film thickness were confirmed by X-ray fluorescence and photoemission spectroscopy. The accuracy of the parameter x was about ± 0.03 for $x=0.16$, ± 0.01 for $x=0.07$, and ± 0.03 for $x=0.03$ sample, which was estimated by comparing XPS and XRF measurements.

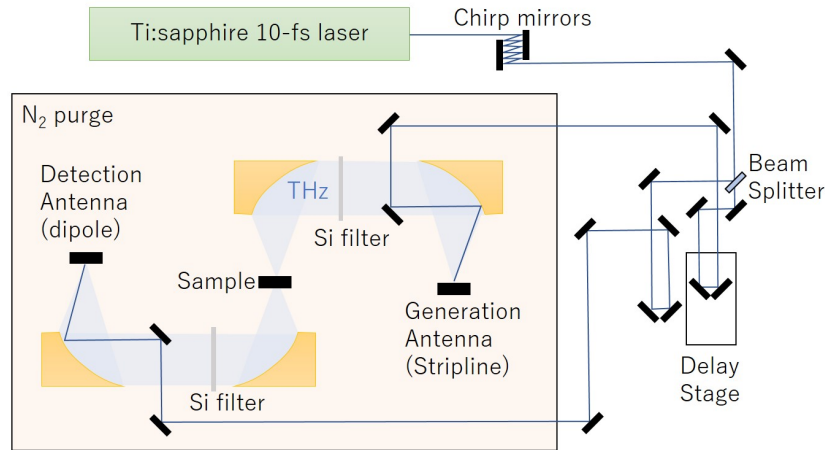


Figure S1. Broadband terahertz time-domain spectroscopy setup. Terahertz waves are generated and detected by photoconducting antennae used in a reflection geometry. The setup was partially purged by nitrogen to avoid the absorption due to water vapor.

2. Linear terahertz spectroscopy setup

Linear terahertz absorption spectrum of the sample was measured by a home-made broadband terahertz time-domain spectroscopy setup (THz-TDS) from 0.1 to 10 THz and Fourier-transform infrared spectrometer (FTIR) from 15 to 50 THz. Figure S1 shows the setup for the THz-TDS. We used a Ti:sapphire oscillator with the pulse duration of 15 fs, center wavelength of 800 nm, and repetition rate of 80 MHz for generate and detect terahertz waves [4]. We used low-temperature-grown GaAs photoconducting antennae purchased from Hamamatsu photonics for terahertz generation and detection. The antennae are placed with a reflection configuration to avoid the bandwidth narrowing due to the terahertz absorption in the antenna substrates. The resultant bandwidth of the detected terahertz wave is from 0.1 THz to 10 THz, with a dip at 8 THz due to the transverse optical phonons of the substrate material GaAs. For the FTIR measurement, we used a commercial spectrometer (Nicolet iS50 widerange FTIR from Thermo Scientific). All the measurements are performed at room

temperature of 300 K.

The terahertz transmittance was analyzed by taking the ratio of transmitted terahertz spectrum through sample T with that through the silicon substrate T_0 . For thin films, we could use the Thinkham formula for the transmittance as,

$$\frac{T}{T_0} = \frac{1}{\sigma d / (n+1)c - 1}.$$

Here, σ is the optical conductivity, d the thickness of the film, n the refractive index of the substrate, c the speed of light. By using the Drude model, the conductivity is given by

$$\sigma = \frac{\omega_p^2}{\gamma + i\omega}.$$

Here, ω_p is the plasma frequency, and γ the damping constant. The plasma frequency is given by the formula,

$$\omega_p^2 = \frac{ne^2}{m\varepsilon_0}.$$

From this equation, we could evaluate the carrier density in the sample. We used the effective mass m of electrons as $0.005m_0$ to obtain the carrier concentration. Here, m_0 is the electron mass, ε_0 the dielectric constant of vacuum, e the charge of an electron. The obtained x dependence of the Drude parameters are shown in the Fig. 1 of the main text.

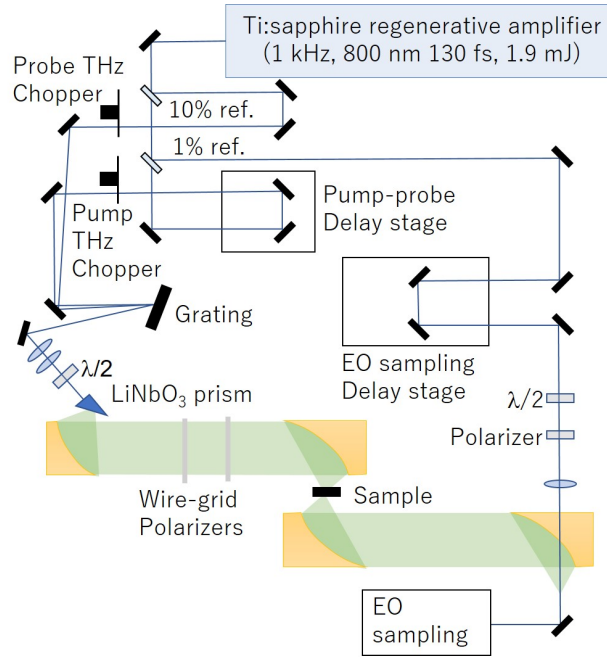


Figure S2. Nonlinear terahertz spectroscopy setup. We used a pair of wire-grid polarizers to control the incident terahertz intensity on the sample, while keeping the polarization.

3. Nonlinear Terahertz spectroscopy setup

To examine terahertz-field-induced nonlinear carrier generation processes in $\text{Bi}_{1-x}\text{Sb}_x$ thin films, we used a Ti:sapphire regenerative amplifier with a repetition rate of 1 kHz, an output power of 2 mJ, a pulse duration of 100 fs and a center wavelength of 800 nm. The intense terahertz wave was generated by a LiNbO_3 prism with a tilted wave-front configuration whose setup is shown in Fig. S2 [5, 6]. The maximum pump terahertz electric-field strength obtained at the sample position was 100 kV/cm, which was enough to induce terahertz nonlinearity in $\text{Bi}_{1-x}\text{Sb}_x$ thin films [7]. For the terahertz detection, we used the electro-optic sampling method with a 0.4 mm (111) GaP crystal.

In the terahertz pump and terahertz probe spectroscopy, we used the similar setup with the nonlinear terahertz spectroscopy, but by exciting the same LiNbO_3 prism using a delay controlled double pulses. In this case, the excitation pulse for the probe terahertz

wave was chopped, and the electro-optic signal that originate from the probe was selectively observed. We note that no nonlinearity of the EO sampling was observed in our experimental configuration.

4. Calculation Procedure

In the calculation of the Zener tunneling probability, we used the bandgap energy E_g and chemical potential μ with the following x dependence.

$$E_g = 0.0154|1 - x/0.04| \text{ [eV]},$$

$$\mu = \begin{cases} 0.0354(1 - x/0.09) & 0 < x < 0.09 \\ 0 & 0.09 < x \end{cases} \text{ [eV]}.$$

The band structure of the L-point was assumed to be hyperbolic for all the antimony concentration. The contribution from the other bands such as the T and H points are neglected because they have much larger effective masses and bandgaps. These values are empirical, and are taken from the reference [8] (figure 2 of the reference).

References

- [1] T. Hirahara, T. Nagao, I. Matsuda, G. Bihlmayer, E.V. Chulkov, Y.M. Koroteev, P.M. Echenique, M. Saito, S. Hasegawa, Phys. Rev. Lett. **97**, 146803 (2006).
- [2] T. Nagao, J.T. Sadowski, M. Saito, S. Yaginuma, Y. Fujikawa, T. Kogure, T. Ohno, Y. Hasegawa, S. Hasegawa, T. Sakurai, Phys. Rev. Lett. **93**, 105501 (2004).
- [3] S. Ito, B. Feng, M. Arita, A. Takayama, R.Y. Liu, T. Someya, W.C. Chen, T. Iimori, H. Namatame, M. Taniguchi, C.M. Cheng, S.J. Tang, F. Komori, K. Kobayashi, T.C. Chiang, I. Matsuda, Phys. Rev. Lett. **117**, 236402 (2016).
- [4] K. Yokota, J. Takeda, C. Dang, G. Han, D.N. McCarthy, T. Nagao, S. Hishita, M. Kitajima, I. Katayama, Appl. Phys. Lett. **100**, 251605 (2012).
- [5] J. Hebling, G. Almási, I.Z. Kozma, J. Kuhl, Opt. Exp. **10**, 1161 (2002).
- [6] H. Hirori, A. Doi, F. Blanchard, K. Tanaka, Appl. Phys. Lett. **98**, 091106 (2011).
- [7] Y. Minami, K. Araki, T.D. Dao, T. Nagao, M. Kitajima, J. Takeda, I. Katayama, Sci. Rep. **5**, 15870 (2015).
- [8] Y. Fuseya, M. Ogata, H. Fukuyama, J. Phys. Soc. Japan **84**, 012001 (2015).